Progress in Natural Science: Materials International 26 (2016) 145–151

HOSTED BY

ELSEVIER

Contents lists available at ScienceDirect

Progress in Natural Science: Materials International

journal homepage: www.elsevier.com/locate/pnsmi

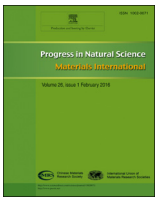

Original Research

Preparation of quantum size of tin oxide: Structural and physical characterization

N.M. Shaalan *, D. Hamad, A.Y. Abdel-Latief, M.A. Abdel-Rahim

Physics Department, Faculty of Science, Assiut University, Assiut 71516, Egypt

ARTICLE INFO

Article history:
Received 11 August 2015
Accepted 28 October 2015
Available online 19 April 2016

Keywords:
Nanostructures
Tin dioxide
Luminescence
Optical properties

ABSTRACT

SnO_2 NPs were successfully prepared via a hydrothermal method. X-ray diffraction analysis confirmed the rutile tetragonal structure of SnO_2 NPs. The crystallite size increased from 1.18 to 5.06 nm with increasing the preparation temperature from 100 to 180 °C. The SEM photography of the products exhibited the agglomeration of the SnO_2 nanocrystals to large view particles, while TEM images confirmed the polycrystalline phase and crystallite size those analyzed from XRD. The UV–vis absorption of ethanol suspended SnO_2 NPs was measured. The optical band-gap energies (E_g) were significantly blue-shifted due to quantum confinement. Fluorescence spectra came to confirm this shift, where a clear shift in the maximum emission peak was observed. Stokes shift of SnO_2 nanocrystals was found to be crystallite size dependent.

1. Introduction

Crystalline semiconductor quantum dots (QDs) have drawn a great attention during the last two decades because of their wide applications such as, nonlinear optical devices, Photoluminescent, electroluminescent phenomena, and medical imaging. The QD is a semiconductor nanostructure that is very small along all three dimensions, implies that the motion of conduction band electrons, valence band holes, and excitons are restricted in three spatial directions [1]. Generally, they have a diameter less than 10 nm, and have dimensions comparable to the exciton Bohr radius. The optical properties could be greatly affected if the size of materials reduced to that of QD. Excitation as well as emission bands can also be controlled by varying the crystallite size. In general, the smaller the diameter, the greater is its exciton binding energy and the higher its emission energy. The size confinement could cause a shift in the band gap of the semiconductor and create excitons with a significant electron-hole binding energy in the excited electronic state [2]. As an example, the band-gap of ZnS is ~3.6 eV for the bulk material, but it can be increased to ~4.5 eV if it is in the form of QDs with a diameter of 1.0 to 4.0 nm [3]. As well, the band gap energy of SnO_2 is ~3.6 eV for the bulk, but it was increased to ~4.35 eV for small SnO_2 NPs [4].

Semiconductor nanostructures have become the focus of intensive research because of their noble properties essentially associated with low dimensionality and size confinement, making the "bottom–up" construction of nanodevices possible [5–7]. Thus, integrating of nanostructures into devices is important and requires new creative methods for nanomaterial fabrication and processing. Tin dioxide, SnO_2, has remarkable physical and chemical properties arising from reducing its dimensionality. Up to date, the researchers are working on reducing the dimensionality of metal oxide, especially SnO_2 because of its wide applications, including solar cell [8], gas sensor [9,10], transparent conducting electrodes [11] and lithium ion battery anode materials [12,13]. For instance, in gas sensing application, by reducing SnO_2 size, we will be able to obtain high gas sensitivity and enhance its performance toward gases [14,15].

In this paper, we successfully synthesized SnO_2 NPs of various sizes less than 10 nm via a hydrothermal method. In this method, the CTAB capping agent and sodium hydroxide as a source of OH^- ions were used. The experiments were carried out in short time of 10 h, compared to others, and at low preparation temperatures, T_A, as well. The obtained products were characterized by XRD, TEM and SEM to investigate their crystallinity and morphology. FTIR spectra were measured for drawing an understanding for a chemical formation of SnO_2 compound. The absorbance and fluorescence (FL) spectra were measured to estimate the band gap energy and the Stokes energy of SnO_2 as a function of the particle size.

2. Experimental details

2.1. Preparation of SnO_2 NPs

SnO_2 NPs were synthesized by a hydrothermal method in the presence of cationic surfactant Cetyl trimethylammonium bromide

* Corresponding author. Tel: +20 88 241 2229
E-mail address: nshaalan@aun.edu.eg (N.M. Shaalan).
Peer review under responsibility of Chinese Materials Research Society.

http://dx.doi.org/10.1016/j.pnsc.2016.03.002

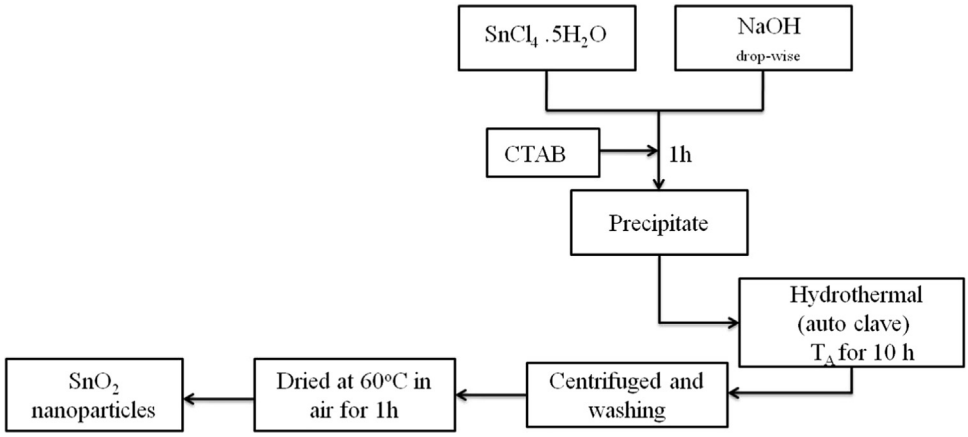

Fig. 1. Flowchart of the synthesis method developed to prepare SnO_2 NPs.

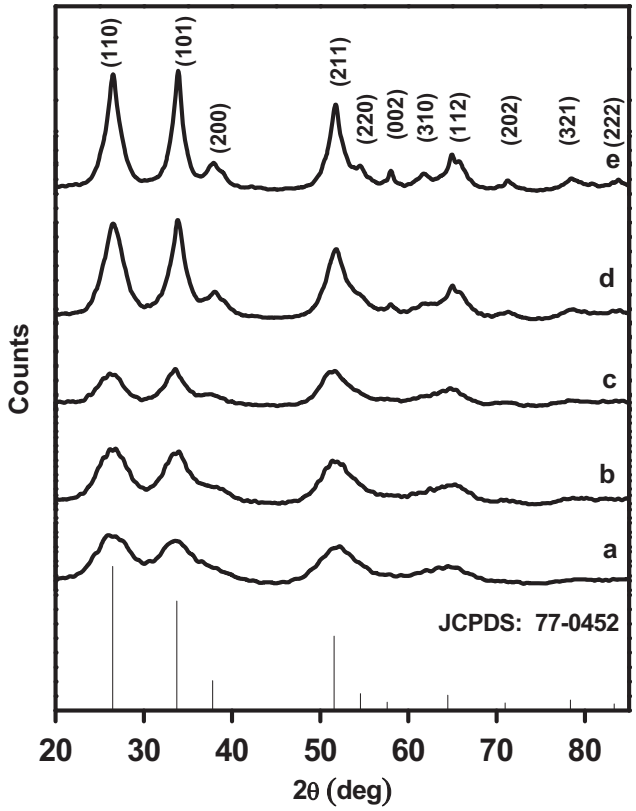

Fig. 2. XRD charts of SnO_2 NPs prepared at T_A: (a) 100, (b) 120, (c) 140, (d) 160, and (e) 180°C.

(CTAB). Typically, 4.532 g of $SnCl_4.5H_2O$ was dissolved in 10 ml of distilled water. As well, 3 g of NaOH were dissolved in 10 ml of distilled water, and then it was added drop-wise to the tin chloride solution under stirring. In addition, 1 g of CTAB was added to the solution under stirring for 1 h. The solution was then poured into a Teflon-lined stainless steel autoclave. The autoclave was sealed and maintained at a prescribed temperature (T_A=100, 120, 140, 160 or 180 °C) for 10 h. Afterward, the autoclave was allowed to cool to the room temperature, resulting in a white precipitate of a product. The white precipitation was then centrifuged and washed several times with a distilled water and absolute ethanol. A simple flowchart of the experimental procedures is shown in Fig. 1.

The chemical reaction mechanisms can normally be expressed as follows. The tin dioxide mesostructure synthesized under acidic conditions is thought to follow the $S^+ X^- I^+$ pathway, where S^+ is the structure director or the CTAB surfactant in this case, I^+ is the inorganic precursor and X^- is the counter ion. Wang et al. [16] proposed a generalized mechanism based on the electrostatic interaction between an inorganic precursor I^+ and a surfactant head group S^+. In this study, I^+ is the stannum ion, Sn^{4+}; S^+ is the surfactant templating agent, CTA^+; and X^- is the halide ion (Cl^-) and the OH^- that serves to buffer the repulsion between the S^+ and I^+ by means of a weak hydrogen bonding force. OH^- is supposed to self-assemble around the cationic surfactant head group molecule (CTA^+), so that the Sn^{4+} ion can be attracted by the assembled OH^- ions to form the mesostructure of tin dioxide [16]. Free OH^- ions remain away from the CTAB molecules and can easily be attracted with Sn^{+4} to form insoluble $Sn(OH)_4$. Eqs. (1) and (2) below describe the possible reaction mechanisms of hydrolysis and condensation, respectively.

Table 1
Standard and observed lattice parameters, *d*-spacing and miller indices.

d-spacing (Å)						*h*	*k*	*l*
Stand. *a*: 4.755 Å, *c*: 3.199 Å	100 °C *a*: 4.711 Å, *c*: 3.205 Å	120 °C *a*: 4.699 Å, *c*: 3.215 Å	140 °C *a*: 4.721 Å, *c*: 3.222 Å	160 °C *a*: 4.748 Å, *c*: 3.183 Å	180 °C *a*: 4.749 Å, *c*: 3.180 Å			
3.364	3.323	3.323	3.405	3.362	3.362	1	1	0
2.655	2.675	2.639	2.671	2.649	2.649	1	0	1
2.378			2.401	2.366	2.366	2	0	0
1.771	1.771	1.778	1.768	1.763	1.763	2	1	1
1.488		1.486	1.488			3	1	0
1.445	1.445	1.444	1.439	1.439	1.439	1	1	2
1.327				1.327	1.327	2	0	2
1.219				1.217	1.217	3	2	1
1.153				1.153	1.153	2	2	2

$$Sn^{4+} + 4OH^- \rightarrow Sn(OH)_4 \quad (1)$$

$$Sn(OH)_4 \rightarrow SnO_2 + 2H_2O \quad (2)$$

where OH^- ions are generated from the decomposition of sodium hydroxide, NaOH and water molecules. After a prolonged process, the colloidal particles will link together to form a resulting network of porous structure.

2.2. SnO_2 nanoparticle characterization

XRD data were carried out with a Philips PW 1700 diffractometer with a copper target and Cu-Kα radiation of λ=1.54056 Å. The sample

Table 2
Crystallite size, lattice parameters, unit volume and number of unit cells of SnO_2 NPs.

Temp. (°C)	100	120	140	160	180
Average crystallite size (nm)	1.81	2.54	2.91	3.52	5.08
Unit cell volume ($Å^3$)	71.17	71.17	71.24	71.69	71.78
Dislocation density (lines/m^2)($\times 10^{15}$)	305.24	155.00	118.09	80.70	38.75
Number of unit cells per crystal.	43.60	120.49	181.02	318.38	955.79

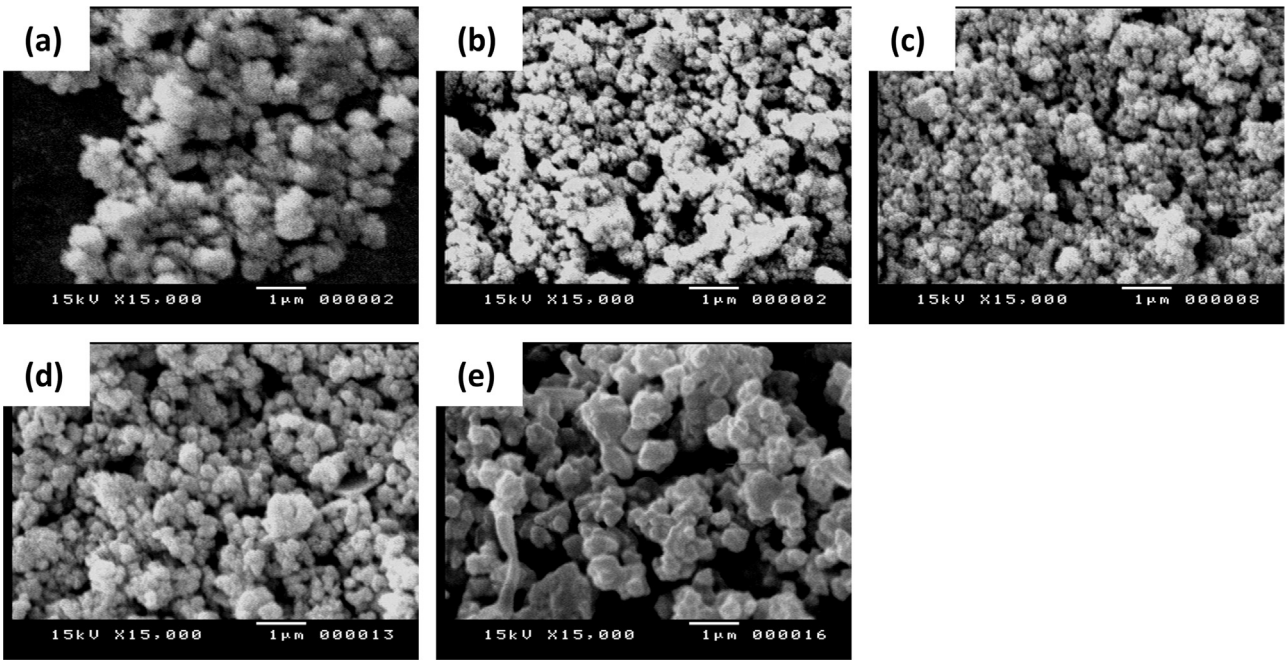

Fig. 3. Low magnification SEM images observed for SnO_2 NPs prepared at T_A: (a) 100, (b) 120, (c) 140, (d) 160, and (e) 180 °C.

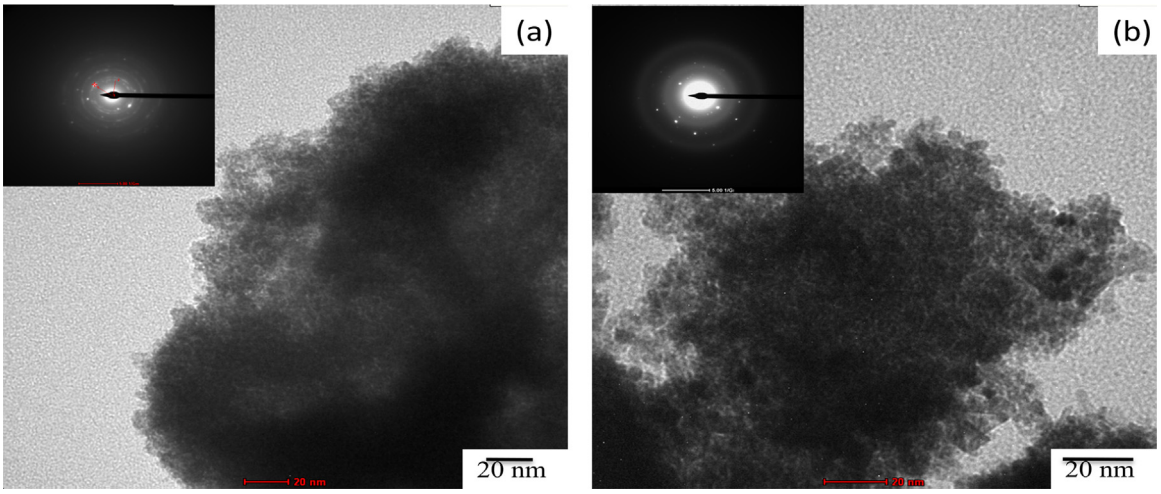

Fig. 4. TEM images, and SAED observed for SnO_2 NPs prepared at (a) 100, and (b) 180 °C.

was scanned from 15° to 90° (2θ) in steps of 0.06 °C/s. FTIR spectra were recorded in the range 400 cm^{-1} to 4000 cm^{-1} by Shimadzu Spectrophotometer (model: Nicolet 6700, using the KBr disk technique). One mg of SnO_2 powder was mixed well with KBr in a mortar and then pressed in a special disc. The crystallinity and surface morphology of the prepared SnO_2 was characterized by TEM (TECNAL G^2 spirit TWIN) and SEM (JEOL, JSM-5400 LV). For TEM specimen SnO_2 powder was suspended in ethanol and then sonicated for 10 min before dropping it onto a carbon coated-copper grid. The absorbance spectra were measured by UV/Vis spectrophotometer (Perkin Elmer, 750 Lamda,) in the range of 200–900 nm. The FL emission spectra were measured by Spectrofluorometer (Jasko, FP-6300 WRE) at room temperature, where SnO_2 NPs were excited by excitation wavelength of 290 nm.

3. Results and discussions

3.1. Crystal structure and morphology of SnO_2

Fig. 2 shows XRD patterns of SnO_2 prepared at different T_A. All diffraction peaks of SnO_2 NPs are matched well with the tetragonal

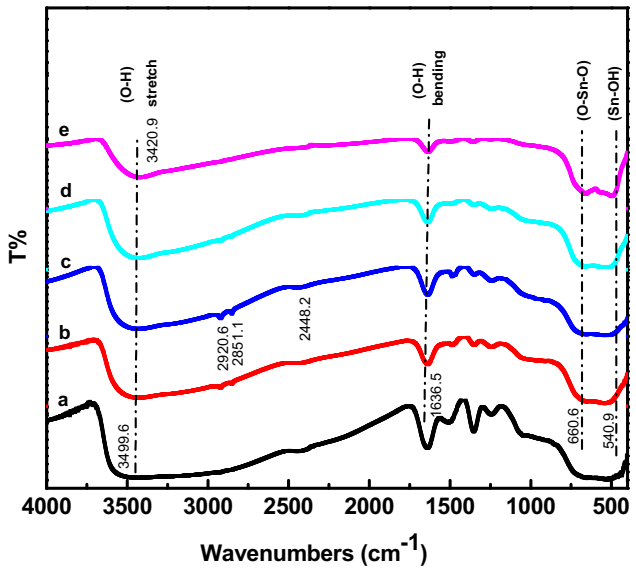

Fig. 5. FTIR Spectra of SnO_2 NPs prepared at T_A: (a) 100, (b) 120, (c) 140, (d) 160, and (e) 180 °C.

rutile structure recorded in JCPDS file no. 77-0452. A small difference in *d*-spacing between the experimental and standard data was observed, especially for the samples prepared at 100 and 120 °C, as listed in Table 1. This difference in *d*-spacing decreased or disappeared for the samples prepared at higher temperatures, indicating the thermal stability of the rutile structure with increasing T_A. No other peaks for any impurities were detected in XRD patterns, indicating the purity and single phase of SnO_2 NPs. At high T_A, an appearance of a new diffraction lines related to the same structure and intense peaks were observed, showing an enhancement of SnO_2 crystallinity. Consequently, the increase in the crystallite size can be identified due to the decrease in the peak's broadening. The variations in the lattice parameters *a* and *c* were also calculated and listed in Table 1. With increasing T_A, the value of *a* parameter increased, while the value of *c* decreased approaches toward the bulk values of SnO_2. The lattice cell volume increased to reach the bulk value (72.34 Å) with increasing T_A. The average crystallite size was calculated by using the Scherrer equation [17]:

$$D = \frac{0.9\lambda}{\beta \cos\theta} \quad (3)$$

where λ is the wavelength of Cu-k_α radiation, θ the Bragg diffraction angle (in radian), and β the integral breadth (i.e. area under the curve divided by maximum height, in radian). The crystallite size was calculated for three most high intensity peaks (110), (101) and (211) and listed in Table 2. The average crystallite size of SnO_2 decreased from 5.06 to 1.81 nm when T_A decreased from 180 to 100 °C.

For more investigation of SnO_2 nanostructure, the dislocation density (δ) and number of unit cell (n) in the particle were calculated and listed in Table 2 using the Eqs. (4) and (5) [18–20]:

$$\delta = \frac{1}{D^2} \quad (4)$$

$$n = \frac{\pi D^3}{6V} \quad (5)$$

where *D* and *V* are the average crystallite size and the cell volume, respectively. The decrease of δ and the increase of n in the particle with increasing T_A may be due to the reducing of defects and the enhancement of crystal growth of SnO_2 NPs.

Fig. 3 shows low magnification SEM images for SnO_2 prepared at various T_A. Individual particles, hardly seen, and agglomerated particles of SnO_2 were observed. Furthermore, the size of these agglomerated particles was increased with increasing T_A. Low-magnification TEM images (Fig. 4) shows SnO_2 NPs synthesized under the conditions of 120 and 180 °C, with a size of approximately 1.8 and 5.0 nm, respectively. Semispherical-like particles can be observed, confirming the particle agglomeration observed in SEM images. The inset electron diffraction pattern taken from the entire NPs demonstrated a polycrystalline phase of these SnO_2 products.

3.2. FTIR spectroscopy

FTIR analysis was carried out within wave numbers of 4000–400 cm^{-1} for SnO_2 prepared at various T_A, as shown in Fig. 5. From FTIR spectra, the band observed in 3420–3499 cm^{-1} and the band observed at 1636 cm^{-1} are assigned to the stretching and bending vibration of the OH group of adsorbed H_2O [21]. These bands are completely different from the coordinated water in the compound [22]. The bands those hardly seen at 2920, 2851, and 2448 cm^{-1} are assigned to C-H stretching and bending vibrations [23,24]. These C–H peaks may be ascribed to the organic residue of CTAB surfactant. The bands observed in 1487–1243 cm^{-1} are assigned to νs (C–O)+δ(O–C=O) [25,26]. It is noticed that the intensities of these peaks decrease with increasing T_A. The peak lies in 525–541 cm^{-1} is related to the terminal oxygen vibration of the Sn–OH [27]. The peak recorded at 660 cm^{-1} is ascribed to O–Sn–O bridge functional group of SnO_2 which confirms the presence of SnO_2 in the crystalline phase [28,29].

3.3. Optical absorbance of SnO_2 NPs

Optical absorbance spectra of SnO_2 prepared at various T_A are shown in Fig. 6. The absorbance edge was shifted to the blue-region with decreasing T_A. We ascribe this shift in the absorbance edge to the decrease in the particle size of SnO_2. The optical direct band gap (E_g) was determined by using Tauc relation by plotting $(\alpha h\upsilon)^{1/r}$ versus $h\upsilon$, (not shown here), where *r* represents the nature of the transition, where $r=1/2$ for the direct allowed transition. The optical band gap energy shifted to the blue region by ~0.4 eV relative to the bulk value of 3.6 eV. Such blue shift might originate due to the quantum confinement associated with the quantum size of SnO_2 NPs [30]. This interpretation is confirmed if the crystallite size is less than or comparable to the Bohr radius of the first excitonic state of SnO_2, which is given by Eq. (6) [31].

$$r_B = \frac{m_0 \varepsilon_r}{\mu} a_B, \quad (6)$$

where m_0 stands for the electron mass, ε_r for the relative dielectric permittivity, μ for the effective reduced electron-hole mass, and a_B for the Bohr radius of the hydrogen atom (5.292×10^{-11} m). For SnO_2, ε_r=14, and the electron effective mass, $m_e^*=0.275m_0$ and the hole effective mass is $m_h^* \ll m_e^*$ (i.e. $\mu=0.275m_0$) [32]. Hence, the calculated diameter, $2r_B$, of SnO_2 is equal to 5.4 nm, which is greater than or comparable with the crystallite size of SnO_2 nanocrystals prepared by the present method, as listed in Table 2.

3.4. FL properties of SnO_2 NPs

FL spectra were carried out in the wavelength range of 310–550 nm with an excitation wavelength of λ_{ex}=290 nm. The emission spectra were recorded for SnO_2 prepared at various T_A, as

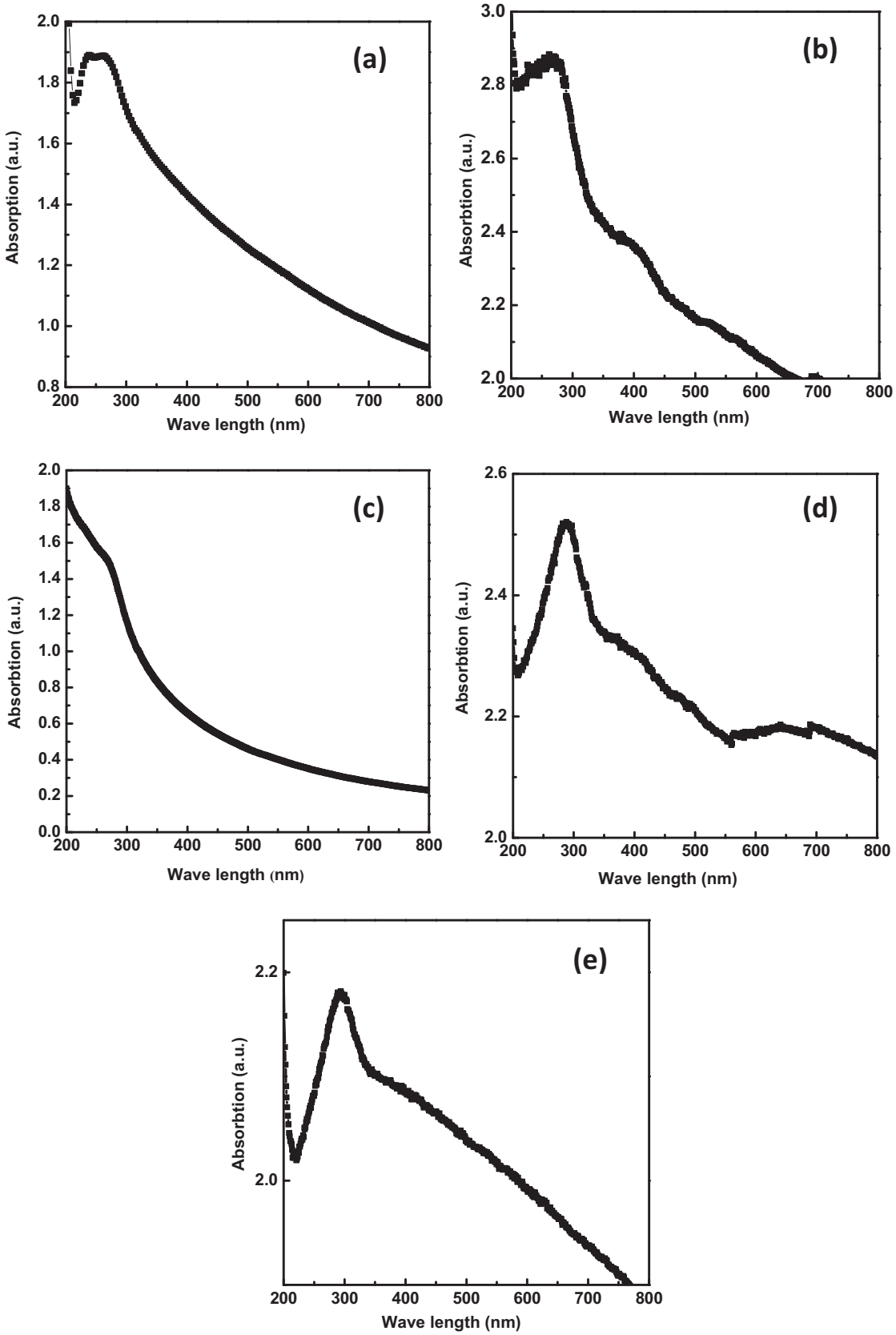

Fig. 6. UV–vis absorbance spectra of the SnO_2 NPs prepared at T_A: (a) 100, (b) 120, (c) 140, (d) 160, and (e) 180 °C.

shown in Fig. 7a. Two emission peaks are consisted in the FL spectra measured for SnO_2. Fig. 7b clearly shows the shift to the high energy region of the maximum emission peak with decreasing T_A. As well, this maximum emission peak was observed at energy higher than that of the bulk material. The maximum emission wavelength, λ_{max}, of the FL spectra was 318.0, 321.3,

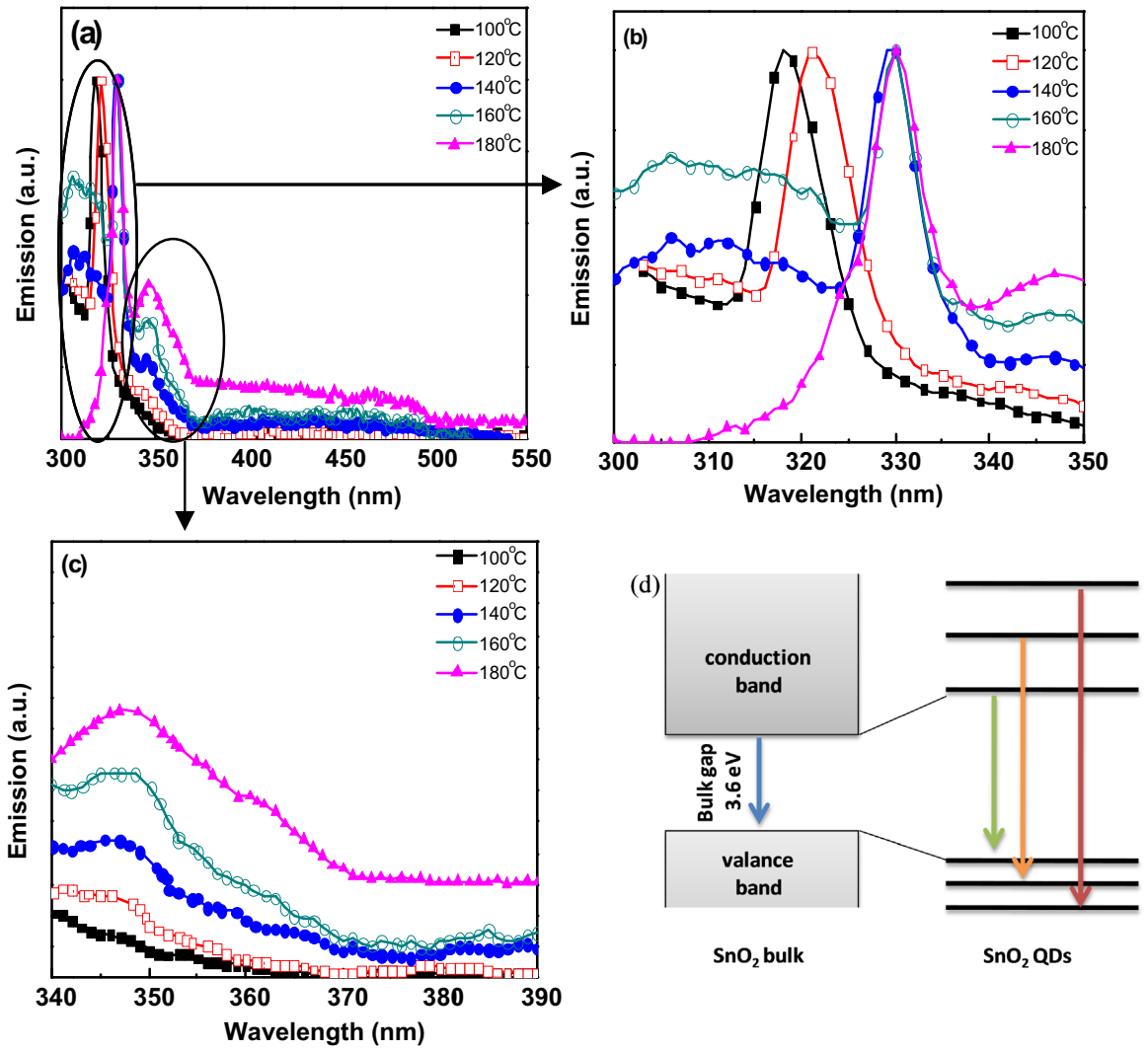

Fig. 7. FL emission spectra at excitation wavelength of 290 nm for SnO_2 NPs prepared at different T_A. (a) Whole range of 300–550 nm, (b) the maximum emission peak in wavelength range of 300–350 nm, (c) the emission peaks observed at 348 nm, and (d) A schematic of the discrete energy level of a semiconductor.

Table 3
The band-gap energy, emission peak wavelength, Stokes shift of SnO_2 NPs.

Temp. (°C)	100	120	140	160	180
Absorbance band-gap energy (eV) ± 0.1	4.05	4.01	3.92	3.70	3.69
Emission peak wavelength (nm)	318.0	321.3	329.1	329.8	330.1
Emission band-gap energy (eV)	3.90	3.86	3.80	3.76	3.75
Stokes shift (eV)	0.859	0.784	0.731	0.504	0.456

329.1, 329.8 and 330.1 nm for SnO_2 NPs prepared at 100, 120, 140, 160 and 180 °C, respectively. The maximum emission wavelength and the corresponding band gap energy are listed in Table 3. One may observe a difference in the value of gap energy calculated from the absorbance spectra and that calculated from the emission spectra. As we mentioned above in Section 3.3 that the band gap energy calculated from the absorbance spectra is based on the fitting line of the absorption edge for $(\alpha h\upsilon)^2$ versus $h\upsilon$. Actually, the correlation factor, R^2, between the fitting line and the selected points of the absorption edge is not exactly equal to 1.0, however, a division error in the calculated band gap energy is about ~0.1 eV. Because of this reason, we observed a difference in the calculated gap energies.

As well known, if the nanocrystals size entered the zone of quantum size, a stronger confinement exists, whereas the carriers are more confined in these nanocrystals [33]. It might result in an increased in the band gap energy. Fig. 7c shows FL emission spectra for an exhibited emission at 348 nm for SnO_2 NPs. The intensity of this emission peak is dependent on T_A. The corresponding band gap energy is 3.56 eV, which is comparable to or less than the band gap energy of SnO_2 bulk. We have a doubt about this peak either ascribed to the bulk due to some unconfined particles or to the contribution of oxygen vacancies and defect in the SnO_2 NPs. However, evidence can be drawn from the intensity of this peak, where its intensity increases with increasing T_A. On the other hand, if T_A decreases from 180 to 120 °C the peak is reduced and disappeared at 100 °C. Furthermore, XRD showed the improvement of SnO_2 crystallinity with increasing T_A, which results in a decrease of the deformation and defect inside the crystals. This can be also drawn from the calculated dislocation density, which decreased with increasing T_A, as listed in Table 2. Thus, all evidences express that this emission peak might originate due to some nanoparticles with size greater than the confined size of 5.4 nm. To gain more insight regarding the FL of SnO_2, a schematic diagram is proposed for the relaxation processes of SnO_2 NPs, as shown in Fig. 7d.

The dependence of the Stokes shift is closely associated with the size of the nanocrystals. Stokes shift of the nanocrystals is

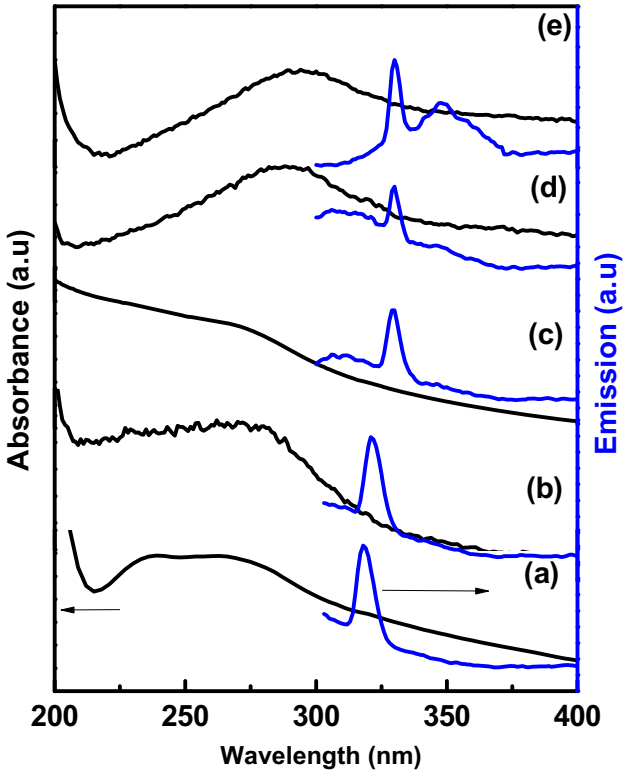

Fig. 8. Stokes shift of SnO_2 NPs prepared at T_A: (a) 100, (b) 120, (c) 140, (d) 160, and (e) 180 °C.

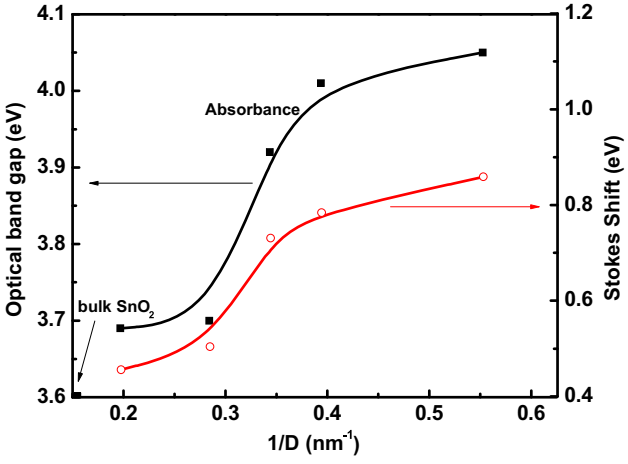

Fig. 9. The band-gap energy and stokes shift (in eV) plotted against the reciprocal diameter of SnO_2 NPs.

defined to be the energy difference between the band-edge absorption peak and the FL peak, when the nanocrystals are excited by photons with energy far above the absorption edge, as shown in Fig. 8. For schemes of quantum confinement, the discrete levels of transition electron become more evident for the difference between the position of peak absorption and emission of the nanocrystals [34,35]. Fig. 9 shows the band-gap energy and Stokes shift versus the reciprocal diameter of the prepared SnO_2 NPs. The values of Stokes shift lie between 0.859 and 0.456 eV and are dependent on the particle size. Both band-gap energy and Stokes shift are proportional to the reciprocal diameter of the particles.

4. Conclusion

In summary, we have successfully prepared SnO_2 NPs in an average size of 1.18–5.06 nm, which is a quantum confinement size (5.4 nm). A hydrothermal method is applied for this purpose, where the experiments were carried out by using a homemade autoclave. These SnO_2 NPs were prepared at low temperatures and short time comparing with the other literature. SnO_2 NPs were characterized by using XRD, FTIR, SEM, and TEM. The optical properties and fluorescence emission spectra clearly demonstrated a good understanding about the band gap energy variation with the quantum size of NPs. The band gap energy of SnO_2 was blue shifted due to the decrease in the particle size. However, the two peaks are observed in the emission spectra; first one has energy higher than that of the bulk material and another has energy compared with the bulk material. The first peak is ascribed to the quantum confinement, where the discrete levels of transition electron become more evident. The latter peak is ascribed to some unconfined particles with a size greater than 5.4 nm. The band-gap energy and Stokes shift are found to be inversely proportional to the nanoparticle size. In conclusion, the band gap energy of SnO_2 NPs can be controlled by the present method. Also, the result suggests that quantum size effect may dominate all aspects of the optical properties of prepared SnO_2 NPs.

References

[1] L. Jacak, P. Hawrylak, A. Wojs, Quantum Dots, Springer Science & Business Media, Technology & Engineering, 2013.
[2] L.E. Brus, J. Chem. Phys. 80 (1984) 4403.
[3] A.A. khosravi, M. Kundu, B.A. Kuruvilla, G.S. Shekhawat, R.P. Gupta, A. K. Sharma, P.D. Vyas, A.K. Kulkarni, Appl. Phys. Lett. 67 (1995) 2506.
[4] A. Gaber, A.Y. Abdel-Latief, M.A. Abdel-Rahim, M.N. Abdel-Salam, Mater. Sci. Semicond. Process. 16 (2013) 1784–1790.
[5] W. Liu, C.M. Lieber, J. Phys. D: Appl. Phys. 39 (2006) R387.
[6] T.J. Kempa, R.W. Day, S. Kim, H. Park, C.M. Lieber, Energy Environ. Sci. 6 (2013) 719.
[7] C. Thelander, P. Agarwal, Mater. Today 9 (2006) 28.
[8] K. Tennakone, J. Bandara, P.K.M. Bandaranayake, G.R.A. Kumara1, A. Konno, Jpn. J. Appl. Phys. 40 (2001) L732.
[9] N.M. Shaalan, T. Yamazaki, T. Kikuta, Sens. Actuators B 153 (2011) 11.
[10] N.M. Shaalan, T. Yamazaki, T. Kikuta, Sens. Actuators B 166–167 (2012) 671.
[11] S. Yu, L. Li, D. Xu, H. Dong, Y. Jin, Solid Films 562 (2014) 501.
[12] S. Li, Q. Wang, W. Xie, S. Xue, X. Hou, D. He, Mater. Lett. 158 (2015) 244.
[13] J. Zhang, L. Chang, F. Wang, D. Xie, Q. Su, G. Du, Mater. Res. Bull. 68 (2015) 120.
[14] M. Agarwal, M.D. Balachandran, S. Shrestha, K. Varahramyan, J. Nanomater. 2012 (2012), Article ID 145406.
[15] S. Seal, S. Shukla, JOM 54 (2002) 35.
[16] Y.D. Wang, C.L. Ma, X.D. Su, H.D. Li, Mater. Lett. 51 (2001) 285–288.
[17] A.R. Stokes, A.C.J. Wilson, Proc. Phys. Soc. 56 (1944) 174.
[18] R. Renugadevi, T. Venkatachalam, R. Narayanasamy, Int. J. Chem. Anal. Sci. 3 (12) (2012) 1648.
[19] V. Senthilkumar, P. Vickraman, J.J. Prince, M. Jayachandran, C. Sanjeeviraja, Philos. Magaz. Lett. 90 (2010) 337.
[20] A. Ayeshamaariam, C. Sanjeeviraja, M. Jayachandran, Int. J. Chem. Anal. Sci. 2 (6) (2011) 54.
[21] Z. Wang, Q. Liu, J. Yu, T. Wu, G. Wang, Appl. Catal. A 239 (2003) 87.
[22] M. Salavati-Niasari, N. Mir, F. Davar, Polyhedron 28 (2009) 1111.
[23] L. Li, Z. Zhu, X. Yao, G. Lu, Z. Yan, Micro. Mes. Mater. 112 (2008) 621.
[24] L. Xi, D. Qian, X. Tang, C. Chen, Mater. Chem. Phys. 108 (2008) 232.
[25] Y. Shimizu, M. Egashira, MRS Bull. 24 (1999) 18.
[26] H.C. Wang, Y. Li, M. Yang, Sens. Actuators B 119 (2006) 380.
[27] S.K. Pillai, L.M. Sikhwivhilu, T.K. Hillie, Mater. Chem. Phys. 120 (2010) 619.
[28] R. Adnan, N.A. Razana, I. Abdul- Rahman, M. Farrukh, J. Chin. Chem. Soc. 57 (2010) 222.
[29] K.C. Song, Y. Kang, Mater. Lett. 42 (2000) 283.
[30] L.E. Brus, J. Phys. Chem. 90 (1989) 2555e2560.
[31] M. Fox, Optical Properties of Solids, Oxford University Press, Oxford 2010, p. 78.
[32] E.J.H. Lee, C. Ribeiro, T.R. Giraldi, E. Longo, E.R. Leite, J.A. Varela, Appl. Phys. Lett. 84 (2004) 1745.
[33] M. Rajalakshmi, A.K. Arora, B.S. Bendre, S. Mahamuni, J. Appl. Phys. 87 (2000) 2445.
[34] N.O. Dantas, P.M.N. de Paula, R.S. Silva, S.V. López-Richard, G.E. Marques, J. Appl. Phys. 109 (2011) 024308.
[35] J. Zhang, X. Jiang, J. Phys. Chem. B 112 (2008) 9557.